

# Hamiltonian engineering of collective XYZ spin models in an optical cavity

Received: 29 March 2024

Accepted: 4 March 2025

Published online: 15 April 2025

 Check for updates

Chengyi Luo<sup>1,2</sup>, Haoqing Zhang<sup>1,2</sup>, Anjun Chu<sup>1</sup>, Chitose Maruko<sup>1</sup>, Ana Maria Rey<sup>1</sup> & James K. Thompson<sup>1</sup>✉

Quantum simulations offer opportunities both for studying many-body physics and for generating useful entangled states. However, existing platforms are usually restricted to specific types of interaction, fundamentally limiting the models they can mimic. Here we realize an all-to-all interacting model with an arbitrary quadratic Hamiltonian, thus demonstrating an infinite-range tunable Heisenberg XYZ model. This was accomplished by engineering cavity-mediated four-photon interactions between an ensemble of 700 rubidium atoms with a pair of momentum states serving as the effective qubit degree of freedom. As one example of the versatility of this approach, we implemented the so-called two-axis counter-twisting model, a collective spin model that can generate spin-squeezed states that saturate the Heisenberg limit on quantum phase estimation. Furthermore, our platform allows for including more than two relevant momentum states by simply adding additional dressing laser tones. This approach opens opportunities for quantum simulation and quantum sensing with matter–wave interferometers and other quantum sensors, such as optical clocks and magnetometers.

The ability to create and control different many-body interactions is key for entanglement generation, optimization, quantum sensing and quantum simulation. Long-range-interacting systems have recently shown much promise for engineering Hamiltonians that generate interesting correlations that propagate across the system. Several experimental platforms are making rapid progress, including Rydberg atoms<sup>1–3</sup>, polar molecules<sup>4,5</sup>, trapped ions<sup>6,7</sup>, cavity quantum-electrodynamic systems<sup>8</sup> and defect centres in solids<sup>9,10</sup>. Short-range contact interactions in ultra-cold atomic systems are another promising approach<sup>11–13</sup>. However, reaching sufficiently low temperatures is an open challenge.

So far, most efforts aimed at engineering Hamiltonians have been limited to XXZ spin models or models that feature both exchange and Ising interactions. Common to these models is that the total magnetization of the spin ensemble is preserved. However, limited progress has been achieved in engineering more general spin models, such as XYZ models, which can break both the SU(2) and U(1) symmetries, that lead to more general ground-state and out-of-equilibrium many-body behaviours. A few exceptions include experiments in Rydberg atoms

using two-colour dressing<sup>14</sup> with dynamics limited to pairs of atoms and Floquet engineering in disordered arrays<sup>2</sup>.

We experimentally show that photon-mediated interactions between atoms inside an optical cavity can be tuned to realize a tunable all-to-all Heisenberg XYZ Hamiltonian, with the added benefit of not requiring the preparation of extremely low-entropy quantum degenerate gases. The interactions are realized using only two dressing lasers in a generalized approach of previous theoretical proposals<sup>15–17</sup>. We benchmarked the tunability of the XYZ Hamiltonian by performing a short-time evolution, which allowed us to characterize the Hamiltonian at the mean-field level by mapping the flow lines on the Bloch sphere. This approach to Hamiltonian engineering can be applied to a wide array of physical systems in which the qubits interact through couplings to a common bosonic mode, including atom–cavity, ion trap and superconducting circuits. The overall performance of the scheme will depend on the details of the physical platform used for the implementation.

As an example of engineering XYZ Hamiltonians, we show that we can transform the previously explored cavity-mediated momentum-exchange interaction  $\hat{J}_+ \hat{J}_- = \hat{\mathbf{J}} \cdot \hat{\mathbf{J}} - \hat{J}_z^2$  (ref. 18) to an all-to-all Ising

<sup>1</sup>JILA, NIST and Department of Physics, University of Colorado, Boulder, CO, USA. <sup>2</sup>These authors contributed equally: Chengyi Luo, Haoqing Zhang.

✉e-mail: [jkt@jila.colorado.edu](mailto:jkt@jila.colorado.edu)

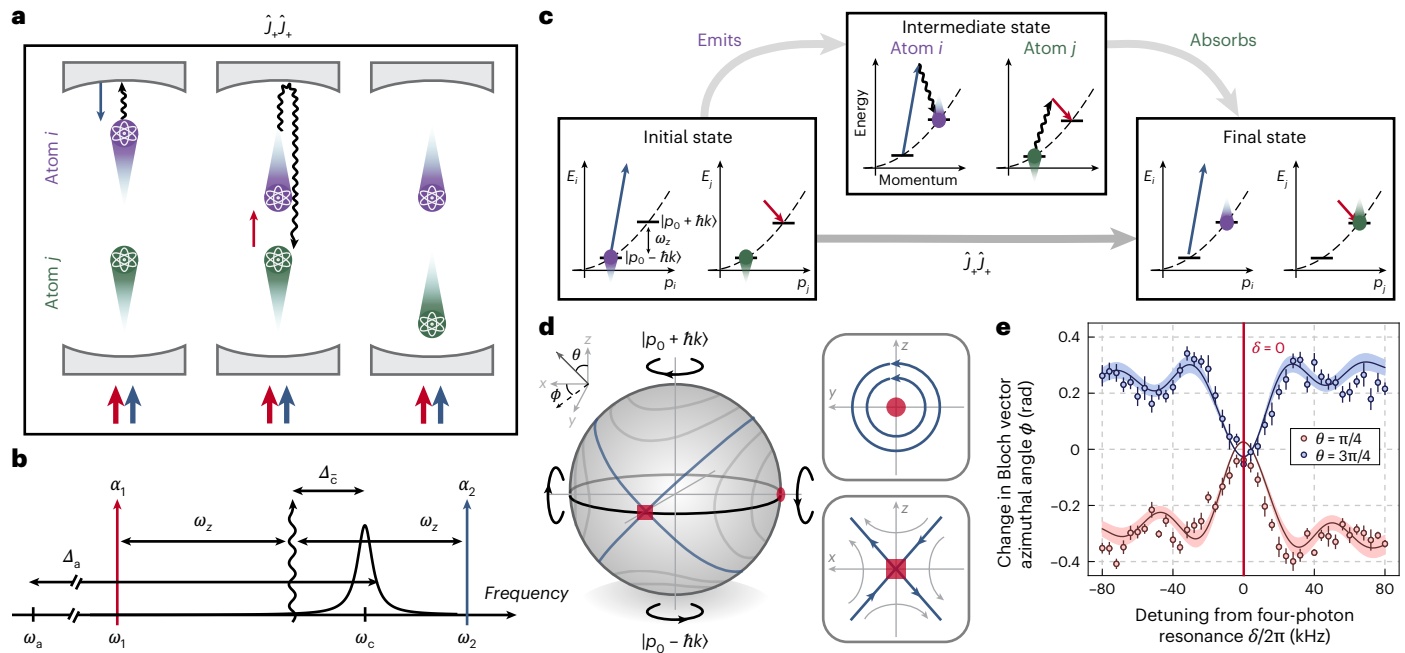


**Fig. 1 | Experimental overview.** **a**, Illustration of the microscopic momentum pair-raising process described by the Hamiltonian  $\hat{J}_+ \hat{J}_+$ , using two momentum states  $p_0 \pm \hbar k$  as a pseudospin-1/2 degree of freedom. Initially, the two atoms *i* and *j* are in the same momentum state along the cavity axis. Dressing lasers are applied to the cavity (red and blue arrows). Atom *i* absorbs a dressing-laser photon and emits a photon (squiggly lines) into the cavity such that the net photon recoil flips its momentum state by  $2\hbar k$ . The emitted photon is absorbed by atom *j*, which also flips its momentum state by  $2\hbar k$ . In the separate momentum-exchange process  $\hat{J}_+ \hat{J}_-$  explored in ref. 18, atoms initially in opposite momentum states flip their momentum states by emitting and absorbing photons. **b**, Frequency diagram of the applied dressing lasers with frequencies  $\omega_{1,2}$  and coherent state amplitudes  $\alpha_{1,2}$ . The emitted photons (squiggly line) are Doppler-shifted by  $\omega_z$  from the dressing-laser frequencies and detuned by  $\Delta_c$  from the cavity resonance frequency  $\omega_c$ . The cavity is far detuned from the atomic transition frequency  $\omega_a$ . **c**, Representation of the emission and absorption processes described in **a** but depicted in terms of the atomic energy versus

momentum for atoms *i* and *j*. The reverse process is also allowed, giving rise to a collective lowering operator described by  $\hat{J}_- \hat{J}_-$ . **d**, Dynamics induced by TACT in the form of a Hamiltonian  $\hat{J}_x^2 - \hat{J}_z^2$  is represented on a Bloch sphere with north and south poles defined by  $|p_0 \pm \hbar k\rangle$ . Top right, local circular flows around the stable point at  $-\hat{x}$ . Bottom right, local flows for unstable saddle points at  $\hat{y}$  with exponential squeezing and anti-squeezing along  $\hat{x} \pm \hat{z}$ . **e**, Observation of the four-photon resonance that generates pair-raising and pair-lowering processes. We scan the dressing-laser frequency difference to vary the detuning  $\delta$ . With equal dressing-laser amplitudes corresponding to realizing the  $\hat{J}_x^2$  Hamiltonian when  $\delta = 0$ , we see clear resonances in the observed change of the azimuthal angle  $\phi$  of a Bloch vector in units of radian (rad) when it is prepared near the south pole ( $\theta = \pi/4$ , red data points) and near the north pole ( $\theta = 3\pi/4$ , blue data points). All error bars reported are  $1\sigma$  uncertainties. Simulation results are shown as solid lines with the shaded area allowing for 5% uncertainty in interaction strength. See Methods for details. For all the Hamiltonians engineered later, we will focus on the resonant case with  $\delta = 0$ , as highlighted by the red solid line.

interaction  $\hat{J}_x^2$ , also known as one-axis twisting (OAT), where  $\hat{J}_+$ ,  $\hat{J}_-$  and  $\hat{J}_{x,y,z}$  are collective pseudospin raising, lowering and projection operators, respectively. This capability allows us to engineer an interaction that we expect to be more robust against collective cavity decay in our atom-cavity platform.

As a second example, we engineered the so-called two-axis counter-twisting (TACT)<sup>19</sup> model. This model was proposed more than 30 years ago<sup>19,20</sup>, but thus far, only the OAT has been realized in experiments, including trapped ions<sup>21,22</sup>, Bose-Einstein condensates<sup>23,24</sup>, atomic cavity quantum electrodynamics<sup>25-29</sup>, superconducting qubits<sup>30</sup> and optical interferometers<sup>31</sup>. Experiments with internal spin degrees of freedom have approximated TACT dynamics with the Holstein-Primakoff approximation (only locally on the Bloch sphere) by combining OAT with a transverse drive (the so-called Lipkin-Meshkov-Glick (LMG) model)<sup>32-35</sup> or equivalent approximations in spin-nematic dynamics in higher spin systems<sup>36,37</sup>. However, there has been no demonstration of TACT in any platform with the exception of a contemporaneous mean-field result using Floquet engineering in an itinerant polar molecule system<sup>38</sup>.

The pseudospin system consists of two momentum states of atoms<sup>39,40</sup> freely falling inside the cavity with an identical internal spin label, making our results of great interest for Bragg matter-wave interferometers<sup>41</sup> that are important for both inertial navigation and fundamental science, such as searches for dark matter and dark energy, detecting gravitational waves and determining the fine structure

constant<sup>42,43</sup>. This approach can also be straightforwardly applied to systems with further internal levels, making it ideal for developing next-generation quantum-enhanced sensors for technology and for exploring a broad range of science from atomic clocks<sup>44,45</sup> and magnetometers<sup>46-48</sup> to geodesy<sup>49</sup>.

## Experimental set-up

In the experiment, <sup>87</sup>Rb atoms were laser-cooled inside a vertically oriented two-mirror standing wave cavity (Fig. 1a)<sup>18,39</sup>. A repulsive intra-cavity doughnut dipole trap confined the atoms radially but allowed the atoms to fall along the cavity axis. To prepare atoms in a well-defined momentum state, a pair of laser beams were injected into the cavity to drive velocity-dependent two-photon Raman transitions between ground hyperfine states  $|F=1, m_F=0\rangle$  and  $|F=2, m_F=0\rangle$ . After removing the unselected atoms with a resonant laser push beam, successive microwave pulses were applied to prepare the internal states of the selected atoms in the ground hyperfine state  $|F=2, m_F=2\rangle$  (Methods)<sup>18</sup>.

With about  $N=700$  atoms centred at momentum  $p_0 - \hbar k$ , another pair of laser beams was injected along the cavity axis to drive two-photon Bragg transitions connecting the two momentum states  $|p_0 \pm \hbar k\rangle$ , which defines a two-level spin-1/2 system<sup>18,39</sup>. The average momentum is  $p_0$ ,  $\hbar$  is the reduced Planck constant and  $k = 2\pi/\lambda$ , where  $\lambda$  is the wavelength of the Bragg laser beams. Ignoring the finite momentum spread of the selected momentum states, we considered

momentum wave packets centred at these two momentum states, as considered in detail previously<sup>18</sup>. We defined  $\hat{\psi}_{\uparrow,\downarrow}^\dagger$  and  $\hat{\psi}_{\uparrow,\downarrow}$  as the operators for creating or annihilating an atom in momentum states  $|\uparrow\rangle \equiv |p_0 + \hbar k\rangle$  and  $|\downarrow\rangle \equiv |p_0 - \hbar k\rangle$ . For mapping to a pseudospin model, we defined ladder operators  $\hat{J}_+ = \hat{\psi}_{\uparrow}^\dagger \hat{\psi}_{\downarrow}$  and  $\hat{J}_- = \hat{\psi}_{\downarrow}^\dagger \hat{\psi}_{\uparrow}$  and spin projection operators  $\hat{J}_x = \frac{1}{2}(\hat{J}_+ + \hat{J}_-)$ ,  $\hat{J}_y = \frac{1}{2i}(\hat{J}_+ - \hat{J}_-)$  and  $\hat{J}_z = \frac{1}{2}(\hat{\psi}_{\uparrow}^\dagger \hat{\psi}_{\uparrow} - \hat{\psi}_{\downarrow}^\dagger \hat{\psi}_{\downarrow})$ .

As shown in Fig. 1b, the cavity frequency  $\omega_c$  was detuned from the atomic transition  $|F=2, m_F=2\rangle \rightarrow |F=3, m_F=3\rangle$  by  $\Delta_a = \omega_c - \omega_a = 2\pi \times 500$  MHz, which is much larger than the excited state decay rate  $\gamma = 2\pi \times 6$  MHz and the cavity power decay rate  $\kappa = 2\pi \times 56(3)$  kHz. A series of Bragg pulses was applied to realize a Mach–Zehnder matter–wave interferometer ( $\pi/2 - \pi - \pi/2$ ), in which the wave packets first separated in position and then re-overlapped. When the two wave packets were overlapping, the interference between them formed an atomic density grating with period  $\lambda/2$ , which matched the standing wave of a cavity mode.

As the atoms moved along the cavity axis, the density grating was periodically aligned to the standing wave of the cavity mode, leading to modulation of the cavity resonance frequency at the two-photon Doppler frequency  $\omega_z = 2kp_0/m \approx 2\pi \times 500$  kHz, where  $m$  is the mass of<sup>87</sup>Rb. To allow this modulation to mediate an effective atom–atom interaction, we typically applied two  $\sigma^+$  polarized dressing-laser tones (Fig. 1a) at frequencies  $\omega_{1,2}$  within a few megahertz of the cavity resonance frequency (Fig. 1b), with complex amplitudes  $\alpha_{1,2}$  corresponding to the field that would be established inside the cavity if there were no atoms in the cavity. The typical values for  $\alpha_{1,2}$  are set to be less than 10 with implicit units  $\sqrt{\text{photons}}$ . The atom-induced cavity frequency modulation led to the generation of modulation sideband tones at frequencies  $\omega_{1,2} \pm \omega_z$ . In the following simplifications, we will assume  $\omega_{1,2} > \omega_z$ .

The key insight is that different combinations of the dressing lasers and their atom-induced sideband tones will induce different virtual four-photon processes, which manifest as all-to-all exchange interactions  $\hat{J}_+ \hat{J}_-$  (ref. 18) and pair-raising  $\hat{J}_+ \hat{J}_+$  (pair-lowering  $\hat{J}_- \hat{J}_-$ ) processes, as shown in Fig. 1a,c. After adiabatically eliminating the cavity fields using second-order perturbation theory (Methods)<sup>18</sup>, we obtained an effective time-dependent atom-only Hamiltonian in an appropriate frame rotating at  $\omega_z$ :

$$\hat{H} = \chi_e \hat{J}_+ \hat{J}_- + \frac{1}{2} (\chi_p e^{i\delta t} \hat{J}_+ \hat{J}_+ + \chi_p^* e^{-i\delta t} \hat{J}_- \hat{J}_-), \quad (1)$$

with the exchange and pair-raising and pair-lowering couplings (for the configuration in Fig. 1b) given by

$$\chi_e = \left( \frac{g_0^2}{4\Delta_a} \right)^2 \left( \frac{|\alpha_1|^2}{\Delta_c + \delta/2} + \frac{|\alpha_2|^2}{\Delta_c - \delta/2} \right), \quad (2)$$

$$\chi_p = \left( \frac{g_0^2}{4\Delta_a} \right)^2 |\alpha_1 \alpha_2| e^{i\phi_{\text{int}}} \left( \frac{1}{\Delta_c + \delta/2} + \frac{1}{\Delta_c - \delta/2} \right).$$

Here,  $\Delta_c = (\omega_2 + \omega_1)/2 - \omega_c$  is the average detuning of the two dressing lasers from cavity resonance, typically set to be less than 1 MHz.  $\delta = (\omega_2 - \omega_1) - 2\omega_z$  is the detuning from four-photon resonance,  $g_0 = 2\pi \times 0.48$  MHz is the maximal atom–cavity Rabi coupling at an antinode of the cavity mode and  $\phi_{\text{int}} = \arg(\alpha_2 \alpha_1^*) - \phi_B$  is the differential phase between the two dressing-laser tones relative to the phase of Bragg coupling  $\phi_B$ , which forms the initial density grating (Methods). The precise derivation of  $\chi_p$  and  $\chi_e$  using a lowest-order Floquet expansion and including cavity decay is discussed in the Methods.

We will focus on the resonant case  $\delta = 0$  and  $\phi_{\text{int}} = 0$ . Although, we show example data in Fig. 1e (Methods) that clearly exhibits a resonance in the interaction-induced dynamics at  $\delta = 0$  as the pair-raising and

pair-lowering processes are tuned into and out of resonance by tuning the dressing-laser frequency difference. In the resonant case, the Hamiltonian of equation (1) reduces to:

$$\begin{aligned} \hat{H} &= (\chi_e + \chi_p) \hat{J}_x^2 + (\chi_e - \chi_p) \hat{J}_y^2 \\ &= \chi_e \hat{\mathbf{J}} \cdot \hat{\mathbf{J}} + \chi_p (\hat{J}_x^2 - \hat{J}_y^2) - \chi_e \hat{J}_z^2, \end{aligned} \quad (3)$$

where we defined the collective angular momentum operator,  $\hat{\mathbf{J}} = \{\hat{J}_x, \hat{J}_y, \hat{J}_z\}$  and introduced the collective Heisenberg interaction  $\hat{\mathbf{J}} \cdot \hat{\mathbf{J}}$ . The latter acts as a constant for any eigenstate of the collective angular momentum operator  $\hat{\mathbf{J}} \cdot \hat{\mathbf{J}}$ , such as the collective states with eigenvalue  $(N/2)(N/2 + 1)$ . In the presence of single-particle inhomogeneities, this term opens a many-body gap that help promote spin-locking, which has previously been explored as protection against the dephasing of coherences stored in internal states<sup>29,50</sup> and in momentum states<sup>18</sup>. We, instead, focused on the fully collective dynamics and, therefore, without loss of generality, we can add a generic  $\chi_z \hat{\mathbf{J}} \cdot \hat{\mathbf{J}}$  term without affecting the dynamics. As such, in our system, we were able to engineer dynamics governed by an XYZ Hamiltonian  $\hat{H} = \chi_x \hat{J}_x^2 + \chi_y \hat{J}_y^2 + \chi_z \hat{J}_z^2$  with interaction strengths  $\chi_x = (\chi_e + \chi_p + \chi_z)$  and  $\chi_y = (\chi_e - \chi_p + \chi_z)$ . The XYZ Hamiltonian was highly tunable by simply adjusting the relative power in the two applied dressing lasers as  $\chi_e$  scales as  $|\alpha_2|^2$  and  $|\alpha_1|^2$  and  $\chi_p$  scales as  $|\alpha_2 \alpha_1|$ .

To realize the XYZ Hamiltonians of Fig. 2 and 3, we applied the two dressing-laser tones separated by  $\Delta_p = \omega_2 - \omega_1 = 2\omega_z \approx 2\pi \times 1$  MHz, and with the average dressing-laser detuning from the cavity set to  $\Delta_c = 2\pi \times 200$  kHz, as shown in Fig. 1. Because the atoms were accelerating due to gravity,  $\omega_z$  changed linearly in time at a rate  $d\omega_z/dt = 2\pi \times 25.11$  kHz  $\text{ms}^{-1}$ . To compensate for this, we linearly ramped the dressing-laser separation at a rate  $d\Delta_p/dt = 2 d\omega_z/dt$ . Similarly, the difference frequency of the applied Bragg coupling tones was ramped at  $d\omega_z/dt$ . For the TACT Hamiltonian dynamics presented in Figs. 2 and 3, the total power of the incident dressing lasers was approximately 200 pW or 900 photons per microsecond to realize an interaction strength of  $\chi_p = 2\pi \times 1.25$  Hz for a typical duration  $dt = 50$   $\mu\text{s}$ , which was shorter than the wave-packet separation time 175  $\mu\text{s}$ .

To benchmark the implementation of a targeted Hamiltonian, we used a short-time evolution, as this allowed us to directly access the Hamiltonian from the propagator,  $\exp(-i dt \hat{H}/\hbar) \approx 1 - i dt \hat{H}/\hbar$ . Starting with different initial conditions, we, thus, studied the linear response of different spin projectors and measured a map of the corresponding flow lines. Besides giving us a direct probe of  $\hat{H}$ , the short-time dynamics has the advantage that it is robust against decoherence and can be studied with a mean-field analysis.

## Mean-field dynamics

At the mean-field level, we defined the Bloch vector  $\mathbf{J} \equiv (J_x, J_y, J_z) = (\langle \hat{J}_x \rangle, \langle \hat{J}_y \rangle, \langle \hat{J}_z \rangle)$  and approximated the Hamiltonian as  $\hat{H} = \mathbf{B}(\mathbf{J}) \cdot \hat{\mathbf{J}}$ . In this way, the collective dynamics are driven by a self-generated effective magnetic field  $\mathbf{B}(\mathbf{J}) = (2\chi_x J_x, 2\chi_y J_y, 2\chi_z J_z)$ , which depends on the instantaneous collective spin projections.

We derived the equations of motion of the collective Bloch vector from equation (3) (Methods), which simplifies to a nonlinear torque equation  $d\mathbf{J}/dt = \mathbf{B}(\mathbf{J}) \times \mathbf{J} \equiv \mathbf{T}(\mathbf{J})$ . One can identify the fixed points  $\mathbf{J}_{\text{fix}}$  as the points where  $\mathbf{T}(\mathbf{J}_{\text{fix}}) = 0$ .

To understand the dynamics near the fixed points, it is useful to follow a standard stability analysis by diagonalizing the Jacobian matrix  $M(\mathbf{J}) = \partial \mathbf{T} / \partial \mathbf{J}|_{\mathbf{J}=\mathbf{J}_{\text{fix}}}$ . The local motion near these fixed points is illustrated in Fig. 1d (right). We used red circles for stable points with purely imaginary eigenvalues. The Bloch vector evolved on stable closed orbits indicated by the blue circular traces. The red squares denote unstable saddle points with real eigenvalues with opposite signs. The eigenvalues of the Jacobian matrix at the saddle points are real but with opposite signs. In

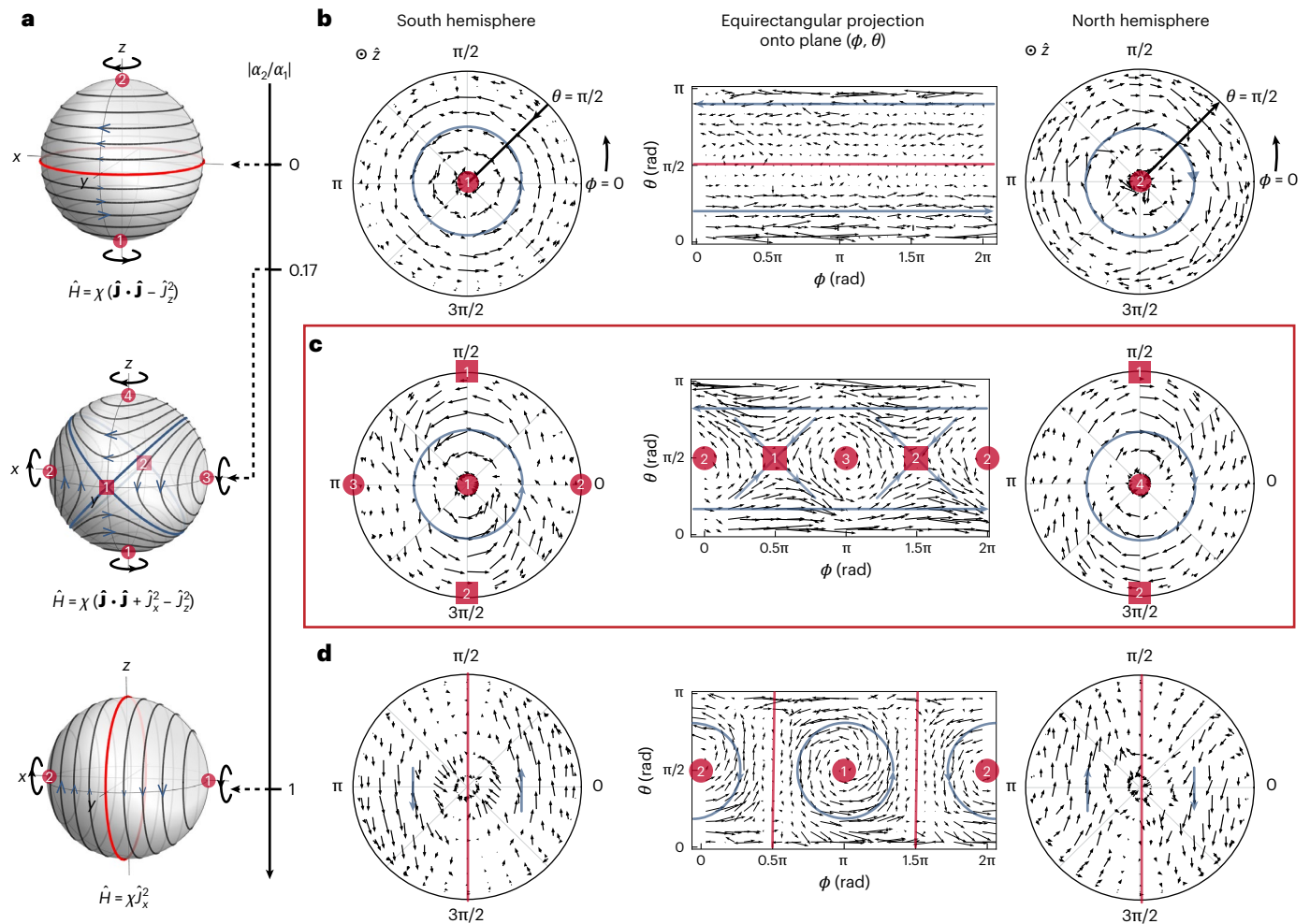


**Fig. 2 | Evolution under different Hamiltonians.** **a**, Setting different amplitude ratios between the two dressing tones  $|\alpha_2/\alpha_1|$  gives rise to different XYZ Hamiltonians, with specific examples shown. **b–d**, The experimentally observed dynamics are shown in the corresponding rows: **(b)** OAT  $\hat{J} \cdot \hat{\mathbf{j}} - \hat{J}_z^2$ , **(c)** TACT  $\hat{\mathbf{J}} \cdot \hat{\mathbf{j}} + \hat{J}_x^2 - \hat{J}_z^2$  and **(d)** OAT  $\hat{J}_x^2$ . The tail of each vector indicates the initial position of the Bloch vector  $\mathbf{J}_i$  on the Bloch sphere, and the arrow indicates the displacement  $\mathbf{T}$  after a brief period of evolution under the corresponding Hamiltonians. The left (right) panels are for initial Bloch vectors on the south (north) hemisphere with azimuthal angle  $\phi$ . The polar angle  $\theta$  of the initial Bloch

vector linearly increases from  $\pi/2$  at the rim to  $\pi$  in the middle for the left plot, whereas  $\theta$  decreases from  $\pi/2$  at the rim to 0 in the middle for the right plot. We believe that the flow lines near the poles deviate from the ideal due to a small systematic offset in the measurements that is magnified near the poles. The middle panels are equirectangular projections. In each case, the qualitatively observed stable fixed points are marked with numbered red circles, and the unstable fixed points are marked with numbered red squares. The blue lines indicate the directions of the observed flow. The red lines indicate where the dynamics are zero and separate regions of opposite flows on the Bloch sphere.

Fig. 1d (bottom right), the dynamics show exponential divergence from the origin (indicated by outward blue arrows) along  $\hat{x} + \hat{z}$ , corresponding to the positive eigenvalue<sup>51</sup>. The negative eigenvalues are indicated by the convergence towards the origin (inward blue arrows) along  $\hat{x} - \hat{z}$ .

### Dynamics on the Bloch sphere

In the experiment, we probed the local dynamics induced by the above Hamiltonian with various values of  $\chi_e$  and  $\chi_p$ . To do this, we varied the phase and duration of the Bragg pulse to prepare an initial pseudospin coherent state  $\mathbf{J}_i$ . Before the atomic wave packets separated, we applied the interaction for a short time  $\Delta t$  satisfying  $\chi N \Delta t \ll 1$  and measured the change in azimuthal angle  $d\phi$  and polar angle  $d\theta$  to obtain the final Bloch vector  $\mathbf{J}_f$  after the interaction. This was achieved by repeating the experiment and applying other appropriate rotations before measuring the populations in the two momentum states (Methods). The local flow vector was then determined by the torque  $\mathbf{T}(\mathbf{J}_i) \approx \Delta \mathbf{J} / \Delta t = (\mathbf{J}_f - \mathbf{J}_i) / \Delta t$ .

Figure 2a shows the predicted flow vectors  $\mathbf{T}(\mathbf{J}_i)$  on the Bloch sphere for three example Hamiltonians of interest. Different Hamiltonians were obtained by changing the ratio of the dressing-laser amplitudes  $|\alpha_2/\alpha_1| = 0, 0.17$  and 1.0.

We show the measured flow vector  $\mathbf{T}(\mathbf{J}_i)$  in Fig. 2b with each row aligned to the corresponding example presented in Fig. 2a. In each case, the flow vector started at  $\mathbf{J}_i$  and ended at  $\mathbf{J}_f$ . The left (right) panels are polar plots (radial coordinate linear in the polar angle) of the dynamics on the south (north) hemisphere looking from the north poles of the Bloch sphere. The middle panels are equirectangular projections to show the dynamics near the equator. From these vector maps, we made qualitative comparisons based on the geometry of the flow. For both the theoretical and experimental results, the stable fixed points and unstable saddle points are labelled as numbered red circles and squares, respectively<sup>51,52</sup>.

In the first row of Fig. 2, we consider the simplest case with  $\chi_p = 0$ . This was achieved by turning off one of the dressing lasers ( $|\alpha_2/\alpha_1| = 0$ ), leading to the Hamiltonian  $\hat{H} = \chi_e (\hat{\mathbf{J}} \cdot \hat{\mathbf{j}} - \hat{J}_z^2)$ . This Hamiltonian, referred to as the OAT Hamiltonian<sup>19</sup>, maintained U(1) symmetry, thereby conserving  $J_z$ . At the mean-field level, it had a constant effective magnetic field along the  $\hat{z}$  direction, which resulted in the rotation of the collective Bloch vector about the  $\hat{z}$  axis at a uniform constant angular frequency,  $-2\chi_e J_z$ . As expected, we observed two stable fixed points (red circles 1 and 2) and a reversal of the circulation across the equator

( $J_z = 0$ ), where there were no dynamics (red line). This  $J_z$ -dependent circulation led to shearing of the quantum noise in the orientation of a Bloch vector on the Bloch sphere, a semiclassical explanation for how OAT dynamics generate spin-squeezed states<sup>19,39</sup>. Note that, although the term  $\hat{\mathbf{J}} \cdot \hat{\mathbf{J}}$  was trivial for our current observations at short times, at longer times, when inhomogeneities in our system manifest, it can lead to important dynamical effects, as shown in ref. 18.

Next, we consider the last row in Fig. 2 with  $\chi_p = \chi_e$ . This was achieved by using equal dressing-laser amplitudes  $|\alpha_2/\alpha_1| = 1$ . Here, the Hamiltonian was  $\hat{H} = 2\chi_e \hat{J}_x^2$ , leading to OAT dynamics along the  $\hat{x}$  direction. The corresponding dynamics were induced at the mean-field level by a magnetic field along  $\hat{x}$  that preserved  $J_x$  and induced a rotation about  $\hat{x}$  with constant angular frequency  $4\chi_e J_x$ . Note that the interaction strength here is twice that of the  $J_z$  case, which is attributed to the use of two dressing-laser tones. The data qualitatively show two stable fixed points along  $\hat{x}$  labelled by red circles 1 and 2 and a reversal of the sign of circulation across  $J_x$ , highlighted by the red lines.

Finally, we come to the case that achieved TACT, as shown in the middle row of Fig. 2. In this case, the ratio of the dressing-laser amplitudes was set to  $|\alpha_2/\alpha_1| = (\sqrt{2} - 1)/(\sqrt{2} + 1) \approx 0.17$ , which produces  $\chi_e = 3\chi_p$ . The Hamiltonian then becomes  $\hat{H} = 2\chi_p(2\hat{J}_x^2 + \hat{J}_y^2) = 2\chi_p(\hat{\mathbf{J}} \cdot \hat{\mathbf{J}} + \hat{J}_x^2 - \hat{J}_z^2)$ .

The corresponding mean-field magnetic field was now  $\mathbf{B}(\mathbf{J}) = 4\chi_p(J_x, 0, -J_z)$ , where we have again ignored the Heisenberg term, as we only consider dynamics at constant Bloch vector length. The theoretical flow line for the dynamics is depicted in Fig. 2a (middle), which shows four stable fixed points along  $\pm\hat{x}$  and  $\pm\hat{z}$  (red circles) as well as two unstable fixed points along  $\pm\hat{y}$  (red squares) connected by great circles inclined at  $\pm\pi/4$  to the equatorial plane. In comparison to OAT, there are two twisting fields. Thus, only the two points at the intersections of the two blue circles with  $J_x = J_z = 0$  exhibit the maximum shearing dynamics, which are the unstable saddle points.

We experimentally explored the flow lines. In the left and right panels of Fig. 2c, the observed stable fixed points are labelled with red circles numbered 1 to 4. The circulations of the flow lines are opposite for stable fixed points on opposite sides of the Bloch sphere. In the middle panel, two unstable points are labelled with red squares 1 and 2. The two unstable fixed points have flow lines that either diverge from them (blue arrows outward) or converge towards them (blue arrows inward), with the two flows orthogonal to each other (see the discussion below). These findings constitute a direct observation of genuine TACT dynamics. Note that for a particular set of parameters of the LMG Hamiltonian, for example when  $\hat{H} = \chi J_z^2 + \delta \hat{J}_y$ , with  $\delta \approx \chi N$ , and when the Bloch vector initially points along the  $\hat{y}$  direction<sup>51,52</sup>, the flow lines can resemble those close to a saddle point of the TACT model (Methods). However, the instability is restricted to this single point, in contrast to the full TACT, which features two independent unstable points.

For a quantitative comparison, we examined the dynamics near the saddle point  $\mathbf{J}_{\text{sad}}$  along the  $\hat{y}$  axis on the Bloch sphere. Figure 3a maps the displacement  $\mathbf{T}(\mathbf{J}_i)$  as a function of the initial Bloch vector orientation  $\mathbf{J}_i = \mathbf{J}_{\text{sad}} + \mathbf{d}\mathbf{J}_i$ . We scanned the initial Bloch vector angles  $\theta_i$  and  $\phi_i$  over a range  $\pm\pi/12$  centred about  $\pi/2$  (about  $\hat{y}$ ) with discrete points sampled using a detailed  $11 \times 11$  grid.

The mean-field equations of motion for the two orthogonal directions  $\hat{n}_{\pm} = (\hat{x} \pm \hat{z})/\sqrt{2}$  are

$$\begin{aligned} \frac{d}{dt}(J_x + J_z) &= 4\chi_p J_y (J_x + J_z), \\ \frac{d}{dt}(J_x - J_z) &= -4\chi_p J_y (J_x - J_z). \end{aligned} \tag{4}$$

For the small range of angles around the  $\hat{y}$  axis sampled in these measurements, we assumed that  $J_y \approx N/2$ , and therefore, we found that the time derivative of the displacement increases linearly with the displacement itself, indicating dynamics that change exponentially over time.

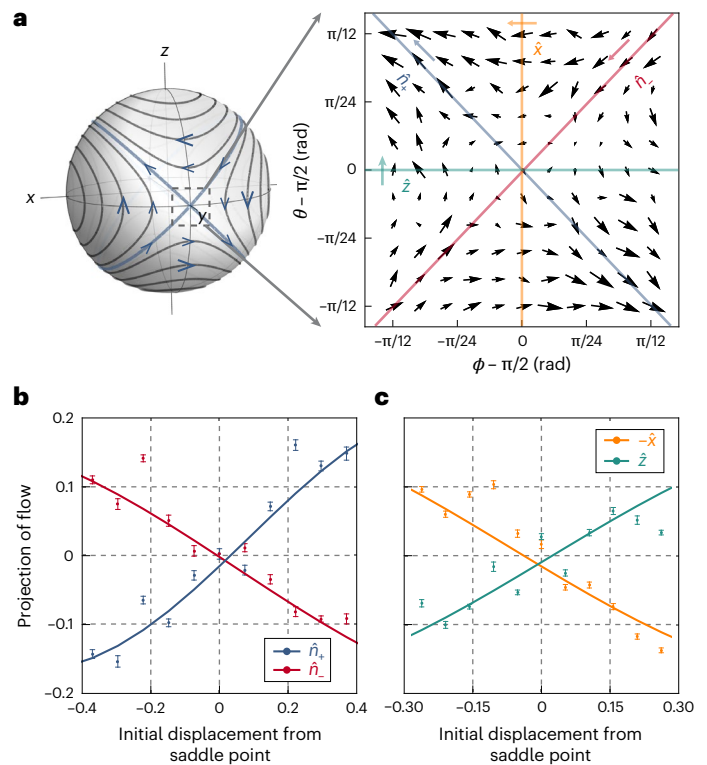


**Fig. 3 | Dynamics near saddle points. a**, Measured local flow vector map around the saddle point for the TACT dynamics. **b**, Blue and red points are parallel projections of the local flow vector onto the  $\hat{n}_{\pm}$  axes  $\Delta\mathbf{J} \cdot \hat{n}_{\pm}/(N/2)$  as a function of initial displacement  $d\mathbf{J}_i \cdot \hat{n}_{\pm}/(N/2)$  from the saddle point along the blue and red lines in **a**. Blue and red solid lines are simulation results. **c**, Green and orange points are the perpendicular projection of the local flow vector as a function of initial angular displacement from the saddle point along the green and orange lines in **a** ( $\hat{n} \times \hat{y} = \hat{z}$  and  $-\hat{x}$  axes ( $\Delta\mathbf{J}_z$  and  $-\Delta\mathbf{J}_x$ )). Orange and green solid lines are simulation results. The observed dynamics near the saddle point are consistent with the exponential growth or decay in the simulation along two orthogonal directions. All error bars in **b** and **c** are  $1\sigma$  uncertainties derived from 15 experimental trials.

Collective or superradiant decay from the cavity introduced another self-generated torque that drove the Bloch vector toward the poles (Methods)<sup>18</sup>. We removed the superradiant dynamics at the lowest order by subtracting a global displacement along  $\hat{z}$  that is common to all data points in Fig. 3 (Methods).

We first focused on the data points along the two directions  $\hat{n}_{\pm}$  (depicted by the blue and red lines in Fig. 3a), and we computed the parallel projection of the flow  $\Delta\mathbf{J} \cdot \hat{n}_{\pm}/(N/2)$  as a function of the initial displacement from the saddle point  $d\mathbf{J}_i \cdot \hat{n}_{\pm}/(N/2)$ , as shown in Fig. 3b. The observed linear relation between the projection of the flow and the initial displacement matches well with the prediction from the simulation results (solid lines), which go beyond the linear approximation by solving the nonlinear equations (Methods). The small differences observed between the  $\Delta\mathbf{J} \cdot \hat{n}_{\pm}/(N/2)$  slopes stem from the finite duration of the interaction, which extends the dynamics beyond the linear response regime.

The unstable dynamics of TACT explain why an initial circular distribution centred around the saddle point shears as a function of time by squeezing (anti-squeezing) along the  $\hat{n}_{-}$  ( $\hat{n}_{+}$ ) direction at a rate exponentially faster than the linear growth seen in OAT. When combined with the global (over the full Bloch sphere) dynamical behaviour, this allowed the TACT to directly approach the fundamental Heisenberg limit on phase estimation<sup>19,51</sup>.

In Fig. 3c, we analyse the orthogonal projection of interaction-induced flows, especially the data points that were initially displaced from

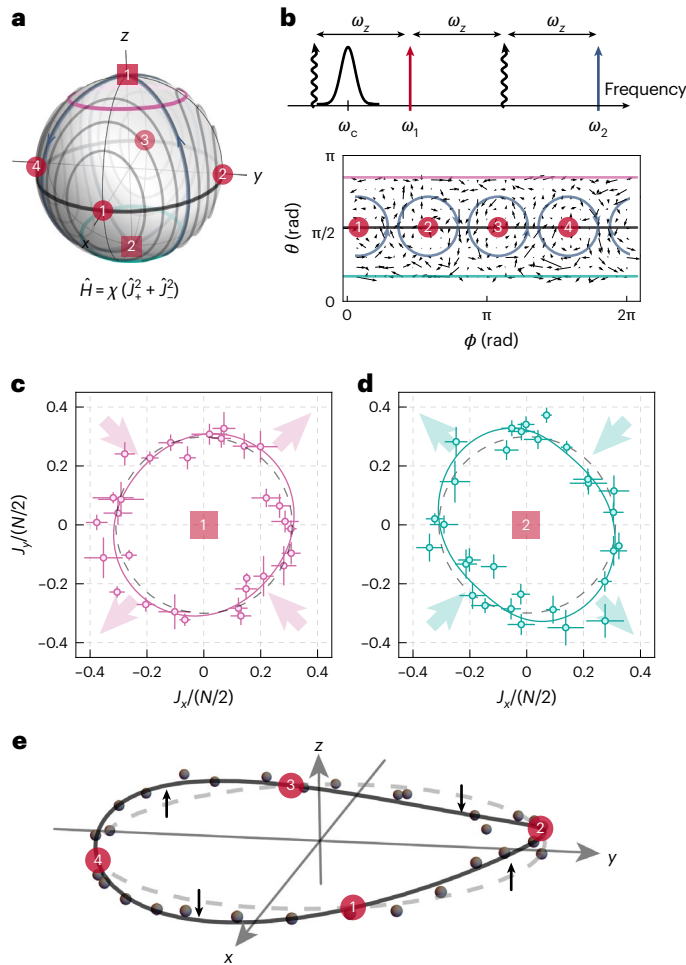


**Fig. 4 | TACT with unstable points at the north and south poles.** **a**, Dynamics shown as flows on the Bloch sphere with three characteristic circles (purple,  $\theta_i = 0.9\pi$ ; black,  $\theta_i = 0.5\pi$  and green,  $\theta_i = 0.1\pi$ ). **b**, Top, frequency diagram with both dressing lasers positioned on the same side relative to the cavity resonance. Bottom, equirectangular projection of the resulting dynamics. **c–e**, Distribution of the states after the interaction with the prepared initial state  $\theta_i = 0.1\pi$  (green circle, **d**),  $0.9\pi$  (purple circle, **c**) and  $0.5\pi$  (black circle, **e**). The deviations from the initial state distribution (grey dashed circles) are shown by the coloured arrows. All error bars presented in **c** and **d** are  $1\sigma$  uncertainties derived from 15 experimental trials.

the saddle point along the  $\hat{n} = \hat{x}$  and  $\hat{z}$  axes (depicted by green and orange lines in Fig. 3a). We calculated their projections along the  $\hat{n} \times \hat{y} = \hat{z}$  and  $-\hat{x}$  axes ( $\Delta\mathbf{J}_z$  and  $-\Delta\mathbf{J}_x$ ), respectively. The dynamics can be explained by noticing that when the Bloch vector was initially prepared in the  $y$ – $z$  plane, the effective mean-field magnetic field was along the  $\hat{z}$  axis with a magnitude of  $-4\chi_p J_z$ . Conversely, when prepared in the  $y$ – $x$  plane, the field was along the  $\hat{x}$  axis with an amplitude of  $4\chi_p J_x$ . Thus, we expected these two perpendicular displacements to grow linearly in magnitude with the initial Bloch vector displacement, as we observed in Fig. 3c.

### TACT with unstable points at the north and south poles

The original TACT Hamiltonian, as proposed by Kitagawa and Ueda<sup>19</sup>, is defined as

$$\hat{H} = \chi(\hat{J}_+^2 + \hat{J}_-^2) = 2\chi(\hat{J}_x^2 - \hat{J}_y^2). \quad (5)$$

The theoretical flow lines are shown in Fig. 4a. This Hamiltonian resembles the previously discussed TACT, with another  $\pi/2$  rotation around

the  $y$  axis. It is characterized by unstable points at the north and south poles of the Bloch sphere, along with four stable points on the equator at  $\pm\hat{x}$  and  $\pm\hat{y}$ . We realized this Hamiltonian by placing the two detuned dressing-laser tones on the same side of the cavity resonance with  $\Delta_c = 2\pi \times 700$  kHz  $> \omega_z$ , such that we needed to account for another modulation sideband with opposite detuning from the cavity resonance, as shown in Fig. 4b (top). In this configuration, the previously ignored lower modulation sideband of the red dressing laser becomes non-negligible. This sideband introduced an exchange interaction with the opposite sign of the other generated exchange interactions. By carefully selecting the detuning and the amplitude ratio of the two dressing-laser tones, we achieved a configuration where  $\chi_e = 0$ , effectively leaving only the  $\chi_p$  term (Methods.) Owing to atom number fluctuations, the dressed cavity resonance also fluctuated, causing the actual value of  $\chi_e$  to fluctuate between positive and negative and average to zero over many runs of the experiment. The r.m.s. value of  $\chi_e$  due to the shot-to-shot error was bounded to be less than 10% of  $\chi_p$  and could be reduced by working with larger cavity detuning from the atomic transition.  $\hat{H}'$  offers the advantage of possibly being less sensitive to the presence of superradiance or collective decay when generating squeezing in our system.

Figure 4b (bottom) shows the measured flow lines for  $\hat{H}'$  in the equirectangular projection. One can clearly identify four stable fixed points on the equator as expected. To provide a better intuition of the dynamics, instead of focusing on the dynamics for the whole Bloch sphere, we took a few cuts with initial Bloch vectors  $\mathbf{J}_i$  prepared with  $\theta_i = 0.1\pi, 0.5\pi$  or  $0.9\pi$  and studied the dynamics separately. For the initial Bloch vectors prepared on the two circles with  $\theta_i = 0.1\pi$  or  $0.9\pi$  (green and purple in Fig. 4a) near the north and south poles, the distributions of the states after the interaction  $\mathbf{J}_f$  are plotted in Fig. 4c,d (solid lines are fitted curves). The elliptical distributions with major axes orthogonal to each other explicitly show the squeezing and anti-squeezing axis near the north and south poles in this small displacement limit. Figure 4e is for the initial Bloch vector prepared on the equator with different azimuthal angles (grey dashed line).  $\mathbf{J}_f$  is plotted with black dots. The four zero crossings correspond to the four stable points on the equator. Between the stable points, the observed final states were deflected alternately above or below the equator, as expected.

### Conclusion

Thus, we have demonstrated the flexibility of our optical cavity simulator when engineering tunable XYZ Hamiltonians using two selected momentum states, without the need for Floquet engineering using discrete rotations. In some cases, it can be challenging for Floquet engineering to gain access beyond mean-field dynamics in large many-body systems due to the increased sensitivity to amplitude and phase noise on the Floquet control fields<sup>53</sup>. We have verified the presence of the pair-raising and pair-lowering processes from the resonant spectroscopic signal when the detuning  $\delta$  was scanned. We also confirmed the direct cancellation of the exchange interactions that yielded the dynamics of the Hamiltonian  $\hat{H}' = \chi(\hat{J}_+^2 + \hat{J}_-^2)$ . By combining the correct relative balance of exchange and pair-raising and pair-lowering contributions, we observed TACT dynamics.

In this work, we focused on characterizing the Hamiltonian by probing the short-time dynamics at the mean-field level. In the future, the capability of engineering a broad range of XYZ models presents exciting opportunities when extending the experiments to longer timescales, where entanglement effects are expected to become manifest. Collective cavity decay and single-particle free-space emissions limit the squeezing attainable in our atom–cavity system. By transforming from  $\mathbf{J} \cdot \mathbf{J} - J_z^2$  (ref. 18) to  $J_x^2$  or TACT, the attainable squeezing variance is expected to improve from  $-1/(NC)^{1/3}$  (ref. 54) to  $-1/(NC)^{1/2}$  (refs. 15,55), where  $C$  is the single-particle cooperativity (Methods). Our system has the potential to achieve above 20 dB (state-of-the-art

levels<sup>56,57</sup>) if the number of atoms is increased to a million, for example, by starting with a Bose–Einstein condensate instead of a thermal gas. Exploring beyond mean-field physics will require improved dressing-laser phase noise, as presently the phase to amplitude noise conversion produced by the cavity induces random deflections of the Bloch vector that mask the entanglement. It will be of great interest to understand the limits of this approach for realizing all-to-all XYZ Hamiltonians when used with other physical platforms, such as ion traps and superconducting circuits, which have different sources of decoherence compared to the present atom–cavity system.

Furthermore, although we have focused on only two momentum states as a first step, by combining them with the actual internal states of the atoms<sup>39,40</sup> or by adding more selected momentum states and dressing tones, one should be able to engineer a toolbox for quantum-state engineering, as has been done with momentum states in Bose–Einstein condensates<sup>58–61</sup>. In our case, however, in addition to the internal and external level control that tunes the synthetic dimensions, we could employ the rich opportunities offered by the tunable cavity-mediated interactions to engineer phenomena ranging from superfluidity and supersolidity<sup>27,62–64</sup> to dynamical gauge fields and non-trivial topological behaviour<sup>8,65–68</sup>.

## Online content

Any methods, additional references, Nature Portfolio reporting summaries, source data, extended data, supplementary information, acknowledgements, peer review information; details of author contributions and competing interests; and statements of data and code availability are available at <https://doi.org/10.1038/s41567-025-02866-0>.

## References

- Browaeys, A. & Lahaye, T. Many-body physics with individually controlled Rydberg atoms. *Nat. Phys.* **16**, 132–142 (2020).
- Geier, S. et al. Floquet Hamiltonian engineering of an isolated many-body spin system. *Science* **374**, 1149–1152 (2021).
- Wu, X. et al. A concise review of Rydberg atom based quantum computation and quantum simulation. *Chin. Phys. B* **30**, 020305 (2021).
- Bohn, J. L., Rey, A. M. & Ye, J. Cold molecules: progress in quantum engineering of chemistry and quantum matter. *Science* **357**, 1002–1010 (2017).
- Li, J.-R. et al. Tunable itinerant spin dynamics with polar molecules. *Nature* **614**, 70–74 (2023).
- Zhang, J. et al. Observation of a discrete time crystal. *Nature* **543**, 217–220 (2017).
- Monroe, C. et al. Programmable quantum simulations of spin systems with trapped ions. *Rev. Mod. Phys.* **93**, 025001 (2021).
- Mivehvar, F., Piazza, F., Donner, T. & Ritsch, H. Cavity QED with quantum gases: new paradigms in many-body physics. *Adv. Phys.* **70**, 1–153 (2021).
- Choi, J. et al. Robust dynamic Hamiltonian engineering of many-body spin systems. *Phys. Rev. X* **10**, 031002 (2020).
- Munns, J. H., Orphal-Kobin, L., Pieplow, G. & Schröder, T. in *Photonic Quantum Technologies: Science and Applications* (ed. Benyoucef, M.) Ch. 19 (Wiley, 2023).
- Bloch, I., Dalibard, J. & Zweger, W. Many-body physics with ultracold gases. *Rev. Mod. Phys.* **80**, 885–964 (2008).
- Schäfer, F., Fukuhara, T., Sugawa, S., Takasu, Y. & Takahashi, Y. Tools for quantum simulation with ultracold atoms in optical lattices. *Nat. Rev. Phys.* **2**, 411–425 (2020).
- Gross, C. & Bloch, I. Quantum simulations with ultracold atoms in optical lattices. *Science* **357**, 995–1001 (2017).
- Steinert, L.-M. et al. Spatially tunable spin interactions in neutral atom arrays. *Phys. Rev. Lett.* **130**, 243001 (2023).
- Sørensen, A. S. & Mølmer, K. Entangling atoms in bad cavities. *Phys. Rev. A* **66**, 022314 (2002).
- Borregaard, J., Davis, E. J., Bentsen, G. S., Schleier-Smith, M. H. & Sørensen, A. S. One- and two-axis squeezing of atomic ensembles in optical cavities. *New J. Phys.* **19**, 093021 (2017).
- Zhang, Y.-C., Zhou, X.-F., Zhou, X., Guo, G.-C. & Zhou, Z.-W. Cavity-assisted single-mode and two-mode spin-squeezed states via phase-locked atom-photon coupling. *Phys. Rev. Lett.* **118**, 083604 (2017).
- Luo, C. et al. Momentum-exchange interactions in a Bragg atom interferometer suppress Doppler dephasing. *Science* **384**, 551–556 (2024).
- Kitagawa, M. & Ueda, M. Squeezed spin states. *Phys. Rev. A* **47**, 5138–5143 (1993).
- Shirasaki, M. & Haus, H. A. Squeezing of pulses in a nonlinear interferometer. *J. Opt. Soc. Am. B* **7**, 30–34 (1990).
- Sackett, C. A. et al. Experimental entanglement of four particles. *Nature* **404**, 256–259 (2000).
- Benhelm, J., Kirchmair, G., Roos, C. F. & Blatt, R. Towards fault-tolerant quantum computing with trapped ions. *Nat. Phys.* **4**, 463–466 (2008).
- Gross, C., Zibold, T., Nicklas, E., Estève, J. & Oberthaler, M. K. Nonlinear atom interferometer surpasses classical precision limit. *Nature* **464**, 1165–1169 (2010).
- Riedel, M. F. et al. Atom-chip-based generation of entanglement for quantum metrology. *Nature* **464**, 1170–1173 (2010).
- Leroux, I. D., Schleier-Smith, M. H. & Vuletić, V. Implementation of cavity squeezing of a collective atomic spin. *Phys. Rev. Lett.* **104**, 073602 (2010).
- Leroux, I. D., Schleier-Smith, M. H. & Vuletić, V. Orientation-dependent entanglement lifetime in a squeezed atomic clock. *Phys. Rev. Lett.* **104**, 250801 (2010).
- Baumann, K., Guerlin, C., Brennecke, F. & Esslinger, T. Dicke quantum phase transition with a superfluid gas in an optical cavity. *Nature* **464**, 1301–1306 (2010).
- Kroeze, R. M., Guo, Y., Vaidya, V. D., Keeling, J. & Lev, B. L. Spinor self-ordering of a quantum gas in a cavity. *Phys. Rev. Lett.* **121**, 163601 (2018).
- Davis, E. J. et al. Protecting spin coherence in a tunable Heisenberg model. *Phys. Rev. Lett.* **125**, 060402 (2020).
- Song, C. et al. Generation of multicomponent atomic Schrödinger cat states of up to 20 qubits. *Science* **365**, 574–577 (2019).
- Kalinin, N. et al. Quantum-enhanced interferometer using Kerr squeezing. *Nanophotonics* **12**, 2945–2952 (2023).
- Muessel, W. et al. Twist-and-turn spin squeezing in Bose-Einstein condensates. *Phys. Rev. A* **92**, 023603 (2015).
- Chaudhury, S. et al. Quantum control of the hyperfine spin of a Cs atom ensemble. *Phys. Rev. Lett.* **99**, 163002 (2007).
- Li, Z. et al. Improving metrology with quantum scrambling. *Science* **380**, 1381–1384 (2023).
- Wang, M. et al. Two-axis-twisting spin squeezing by multipass quantum erasure. *Phys. Rev. A* **96**, 013823 (2017).
- Hamley, C. D., Gerving, C. S., Hoang, T. M., Bookjans, E. M. & Chapman, M. S. Spin-nematic squeezed vacuum in a quantum gas. *Nat. Phys.* **8**, 305–308 (2012).
- Luo, X.-Y. et al. Deterministic entanglement generation from driving through quantum phase transitions. *Science* **355**, 620–623 (2017).
- Miller, C. et al. Two-axis twisting using Floquet-engineered XYZ spin models with polar molecules. *Nature* **633**, 332–337 (2024).
- Greve, G. P., Luo, C., Wu, B. & Thompson, J. K. Entanglement-enhanced matter-wave interferometry in a high-finesse cavity. *Nature* **610**, 472–477 (2022).
- Finger, F. et al. Spin- and momentum-correlated atom pairs mediated by photon exchange and seeded by vacuum fluctuations. *Phys. Rev. Lett.* **132**, 093402 (2024).

41. Giltner, D. M., McGowan, R. W. & Lee, S. A. Atom interferometer based on Bragg scattering from standing light waves. *Phys. Rev. Lett.* **75**, 2638–2641 (1995).
42. Parker, R. H., Yu, C., Zhong, W., Estey, B. & Müller, H. Measurement of the fine-structure constant as a test of the standard model. *Science* **360**, 191–195 (2018).
43. Morel, L., Yao, Z., Cladé, P. & Guellati-Khélifa, S. Determination of the fine-structure constant with an accuracy of 81 parts per trillion. *Nature* **588**, 61–65 (2020).
44. Pedrozo-Peñafiel, E. et al. Entanglement on an optical atomic-clock transition. *Nature* **588**, 414–418 (2020).
45. Robinson, J. M. et al. Direct comparison of two spin-squeezed optical clock ensembles at the  $10^{-17}$  level. *Nat. Phys.* **20**, 208–213 (2024).
46. Wasilewski, W. et al. Quantum noise limited and entanglement-assisted magnetometry. *Phys. Rev. Lett.* **104**, 133601 (2010).
47. Koschorreck, M., Napolitano, M., Dubost, B. & Mitchell, M. W. Sub-projection-noise sensitivity in broadband atomic magnetometry. *Phys. Rev. Lett.* **104**, 093602 (2010).
48. Muessel, W., Strobel, H., Linnemann, D., Hume, D. B. & Oberthaler, M. K. Scalable spin squeezing for quantum-enhanced magnetometry with Bose-Einstein condensates. *Phys. Rev. Lett.* **113**, 103004 (2014).
49. McGrew, W. et al. Atomic clock performance enabling geodesy below the centimetre level. *Nature* **564**, 87–90 (2018).
50. Norcia, M. A. et al. Cavity-mediated collective spin-exchange interactions in a strontium superradiant laser. *Science* **361**, 259–262 (2018).
51. Muñoz Arias, M. H., Deutsch, I. H. & Poggi, P. M. Phase-space geometry and optimal state preparation in quantum metrology with collective spins. *PRX Quantum* **4**, 020314 (2023).
52. Kajtoch, D. & Witkowska, E. Quantum dynamics generated by the two-axis counter-twisting Hamiltonian. *Phys. Rev. A* **92**, 013623 (2015).
53. Chen, Z., Bohnet, J. G., Weiner, J. M. & Thompson, J. K. General formalism for evaluating the impact of phase noise on Bloch vector rotations. *Phys. Rev. A* **86**, 032313 (2012).
54. Hu, J. et al. Vacuum spin squeezing. *Phys. Rev. A* **96**, 050301 (2017).
55. Borregaard, J., Davis, E., Bentsen, G. S., Schleier-Smith, M. H. & Sørensen, A. S. One- and two-axis squeezing of atomic ensembles in optical cavities. *New J. Phys.* **19**, 093021 (2017).
56. Hosten, O., Engelsens, N. J., Krishnakumar, R. & Kasevich, M. A. Measurement noise 100 times lower than the quantum-projection limit using entangled atoms. *Nature* **529**, 505 (2016).
57. Cox, K. C., Greve, G. P., Weiner, J. M. & Thompson, J. K. Deterministic squeezed states with collective measurements and feedback. *Phys. Rev. Lett.* **116**, 093602 (2016).
58. Meier, E. J., An, F. A. & Gadway, B. Observation of the topological soliton state in the Su–Schrieffer–Heeger model. *Nat. Commun.* **7**, 13986 (2016).
59. An, F. A., Meier, E. J., Ang’ong’a, J. & Gadway, B. Correlated dynamics in a synthetic lattice of momentum states. *Phys. Rev. Lett.* **120**, 040407 (2018).
60. Meier, E. J. et al. Observation of the topological Anderson insulator in disordered atomic wires. *Science* **362**, 929–933 (2018).
61. An, F. A. et al. Nonlinear dynamics in a synthetic momentum-state lattice. *Phys. Rev. Lett.* **127**, 130401 (2021).
62. Léonard, J., Morales, A., Zupancic, P., Esslinger, T. & Donner, T. Supersolid formation in a quantum gas breaking a continuous translational symmetry. *Nature* **543**, 87–90 (2017).
63. Léonard, J., Morales, A., Zupancic, P., Donner, T. & Esslinger, T. Monitoring and manipulating Higgs and Goldstone modes in a supersolid quantum gas. *Science* **358**, 1415–1418 (2017).
64. Schuster, S., Wolf, P., Ostermann, S., Slama, S. & Zimmermann, C. Supersolid properties of a Bose-Einstein condensate in a ring resonator. *Phys. Rev. Lett.* **124**, 143602 (2020).
65. Ritsch, H., Domokos, P., Brennecke, F. & Esslinger, T. Cold atoms in cavity-generated dynamical optical potentials. *Rev. Mod. Phys.* **85**, 553–601 (2013).
66. Landini, M. et al. Formation of a spin texture in a quantum gas coupled to a cavity. *Phys. Rev. Lett.* **120**, 223602 (2018).
67. Rosa-Medina, R. et al. Observing dynamical currents in a non-Hermitian momentum lattice. *Phys. Rev. Lett.* **128**, 143602 (2022).
68. Colella, E., Kosior, A., Mivehvar, F. & Ritsch, H. Open quantum system simulation of Faraday’s induction law via dynamical instabilities. *Phys. Rev. Lett.* **128**, 070603 (2022).

**Publisher’s note** Springer Nature remains neutral with regard to jurisdictional claims in published maps and institutional affiliations.

This is a U.S. Government work and not under copyright protection in the US; foreign copyright protection may apply 2025

## Methods

### Derivation of Hamiltonian with two-colour couplings

We begin by considering the dispersive atom–cavity coupling Hamiltonian, with the excited state adiabatically eliminated as detailed in ref. 18. By applying two dressing lasers with frequencies  $\omega_{1,2}$  and amplitudes  $\epsilon_{1,2}$  in the rotating frame of the dressed cavity defined by  $\hat{H}_c = \omega_c \hat{a}^\dagger \hat{a}$ , where  $\hat{a}$  and  $\hat{a}^\dagger$  are the cavity field operators, the atom–cavity Hamiltonian can be written as:

$$\begin{aligned} \hat{H}_0 = & \omega_z \hat{J}_z + \frac{g_0^2}{4\Delta_a} \hat{a}^\dagger (\hat{J}_+ + \hat{J}_-) \\ & + \epsilon_1 e^{-i(\omega_1 - \omega_c)t} \hat{a}^\dagger + \epsilon_2 e^{-i(\omega_2 - \omega_c)t} \hat{a}^\dagger + \text{h.c.}, \end{aligned} \quad (6)$$

with the atom–cavity detuning  $\Delta_a = \omega_a - \omega_c$ . In addition, the cavity dissipation can be modelled by a Lindblad operator  $\mathcal{L} = \sqrt{\kappa} \hat{a}$  with  $\kappa$  denoting the cavity decay rate.

We can decompose the cavity field operator into  $\hat{a} = \alpha(t) + \hat{b}$ , where  $\alpha(t)$  represents an oscillating classical field. This field is described by

$$\begin{aligned} \alpha(t) = & \alpha_1 e^{-i(\omega_1 - \omega_c)t} + \alpha_2 e^{-i(\omega_2 - \omega_c)t}, \\ \alpha_1 = & \frac{\epsilon_1}{i\kappa/2 + (\omega_1 - \omega_c)}, \\ \alpha_2 = & \frac{\epsilon_2}{i\kappa/2 + (\omega_2 - \omega_c)}, \end{aligned} \quad (7)$$

where  $\alpha_1$  and  $\alpha_2$  are the complex amplitudes of coherence field inside the cavity as established by the two dressing lasers. We define the detuning for the two dressing lasers as  $\Delta_{c1} = (\omega_1 - \omega_c) + \omega_z$  and  $\Delta_{c2} = (\omega_2 - \omega_c) - \omega_z$ . Additionally, the average detuning and the differential detuning introduced in the main text can now be expressed as  $\Delta_\epsilon = (\Delta_{c1} + \Delta_{c2})/2$  and  $\delta = \Delta_{c2} - \Delta_{c1}$ . The resonance frequency diagram depicted in Fig. 1c illustrates the case when  $\Delta_{c1} = \Delta_{c2} = \Delta_\epsilon < 0$ .

To derive the atom-only dynamics, we applied the standard second-order perturbation theory to eliminate quantum fluctuation  $\hat{b}$ , assuming the negligible excitation  $\langle \hat{b}^\dagger \hat{b} \rangle \ll 1$ . This approach essentially aligns with first-order Floquet or time-average Hamiltonian theory, as we ignore the fast rotating term. The effective Hamiltonian takes the form

$$\begin{aligned} \hat{H}_{\text{eff}}/\hbar = & \left( \frac{g_0^2}{4\Delta_a} \right)^2 \left[ \frac{\Delta_{c1} |\alpha_1|^2}{\Delta_{c1}^2 + (\kappa/2)^2} + \frac{\Delta_{c2} |\alpha_2|^2}{\Delta_{c2}^2 + (\kappa/2)^2} \right] \hat{J}_+ \hat{J}_- \\ & + \left( \frac{g_0^2}{4\Delta_a} \right)^2 \frac{\alpha_2^* \alpha_1}{2} \left( \frac{1}{\Delta_{c1} + i\kappa/2} + \frac{1}{\Delta_{c2} - i\kappa/2} \right) e^{i\delta t} \hat{J}_+ \hat{J}_+ \\ & + \left( \frac{g_0^2}{4\Delta_a} \right)^2 \frac{\alpha_1^* \alpha_2}{2} \left( \frac{1}{\Delta_{c1} - i\kappa/2} + \frac{1}{\Delta_{c2} + i\kappa/2} \right) e^{-i\delta t} \hat{J}_- \hat{J}_-. \end{aligned} \quad (8)$$

Simultaneously, the dissipation is described by the effective Lindblad operator:

$$\hat{\mathcal{L}}_{\text{eff}} = \frac{g_0^2}{4\Delta_a} \sqrt{\kappa} \left[ \frac{\alpha_1 e^{-i\Delta_{c1}t}}{\Delta_{c1} + i\kappa/2} \hat{J}_+ + \frac{\alpha_2 e^{-i\Delta_{c2}t}}{\Delta_{c2} + i\kappa/2} \hat{J}_- \right]. \quad (9)$$

We have ignored two further modulation sidebands that are detuned from the dressed cavity frequency by  $\Delta_{c1} - 2\omega_z$  and  $\Delta_{c2} + 2\omega_z$  (ref. 18), as their contribution to the dynamics is negligible. For the dressing-laser configuration in Fig. 4b, one of the modulation sidebands with detuning  $\Delta_{c1} - 2\omega_z \lesssim \Delta_\epsilon$  from the dressed cavity resonance becomes non-negligible. This sideband introduces another exchange process into the effective Hamiltonian with an opposite sign to that of  $\chi_e$ . To use

that term to obtain the TACT Hamiltonian  $\hat{H}'$  by cancelling the exchange interaction term, we require:

$$\frac{\Delta_{c1} |\alpha_1|^2}{\Delta_{c1}^2 + (\kappa/2)^2} + \frac{\Delta_{c2} |\alpha_2|^2}{\Delta_{c2}^2 + (\kappa/2)^2} = \frac{(\Delta_{c1} - 2\omega_z) |\alpha_1|^2}{(\Delta_{c1} - 2\omega_z)^2 + (\kappa/2)^2}, \quad (10)$$

which was used for the measurements reported in Fig. 4.

For the short-time dynamics explored in Figs. 2 and 4, we ignored the superradiant dynamics given by equation (9) and considered only Hamiltonian evolution. In Fig. 3, to study the slow dynamics near the unstable saddle point, both the experimental data and the theoretical simulation account for and subtract the effects due to superradiance with the same analysis as discussed below.

### Mean-field equation of motion and stability analysis

In this section, we study the fixed points and stability for the general XYZ model in equation (3) and for the LMG model. We start with the mean-field equations of motion for the XYZ model in the Heisenberg picture,

$$\begin{aligned} \frac{dJ_x}{dt} = & 2\chi_y J_y J_z, \\ \frac{dJ_y}{dt} = & -2\chi_x J_x J_z, \\ \frac{dJ_z}{dt} = & 2(\chi_x - \chi_y) J_x J_y, \end{aligned} \quad (11)$$

with  $\chi_x = \chi_e + \chi_p$  and  $\chi_y = \chi_e - \chi_p$  for our realization. The fixed points  $\mathbf{J}_{\text{fix}}$  for the aforementioned nonlinear equations correspond to the spin aligned along the  $\pm x$ ,  $\pm y$  and  $\pm z$  directions. The torque is given by  $\mathbf{T}(\mathbf{J}) = (2\chi_y J_z, -2\chi_x J_z, 2(\chi_x - \chi_y) J_x J_y)$ . The stability at the fixed point can be deduced from the Jacobian matrix,

$$M(\mathbf{J}) = \begin{pmatrix} 0 & 2\chi_y J_z & 2\chi_y J_y \\ -2\chi_x J_z & 0 & -2\chi_x J_x \\ 2(\chi_x - \chi_y) J_y & 2(\chi_x - \chi_y) J_x & 0 \end{pmatrix}. \quad (12)$$

In the dressing-laser configuration depicted in Fig. 1c, we considered the condition where  $\chi_x \leq \chi_y \leq 0$ . Under this configuration,  $\pm x$  and  $\pm z$  represent the stable points of the system, having eigenvalues of  $\pm 2\sqrt{\chi_x(\chi_x - \chi_y)}$  and  $\pm 2\sqrt{\chi_x \chi_y}$ , respectively. Conversely,  $\pm y$  are identified as the saddle points of the system, characterized by the real eigenvalues  $\pm 2\sqrt{\chi_y(\chi_x - \chi_y)}$ . By fixing  $\chi_x$ , the system achieved its largest eigenvalue when  $\chi_y = \chi_x/2$ . Thus,  $\chi_e = 3\chi_p$  corresponds to the TACT Hamiltonian  $\hat{H} = \chi_p (2J_x^2 + J_y^2)$ .

We now apply the same analysis to the LMG model  $\hat{H} = \chi J_z^2 + \delta J_y$  with equations of motion given by,

$$\begin{aligned} \frac{dJ_x}{dt} = & -2\chi J_y J_z + \delta J_z, \\ \frac{dJ_y}{dt} = & 2\chi J_x J_z, \\ \frac{dJ_z}{dt} = & -\delta J_x. \end{aligned} \quad (13)$$

Following the previously outlined procedure, we identified two stable points at  $\mathbf{J}_{\text{fix}} = \frac{N}{2} (0, \delta/\chi N, \pm \sqrt{1 - (\delta/\chi N)^2})$ , one stable point along the  $-y$  direction and one saddle point along the  $y$  direction, given  $0 < \delta < \chi N$ . When  $\delta > \chi N$ , the system had two stable points along the  $\pm y$  directions and no saddle points. The eigenvalues of the Jacobian matrix at the saddle point were  $\pm \chi N \sqrt{\delta/\chi N (1 - \delta/\chi N)}$ , and for fixed  $\chi N$ , the maximum rate was achieved when  $\delta/\chi N = 1/2$ .

After examining the global flow lines, which revealed notable differences between the TACT and LMG models as previously discussed, we now shift our focus to the local flow lines near the saddle point along the  $\hat{y}$  direction. We analysed this using the Holstein–Primakoff approximation, in which the spin operators are represented as  $\hat{J}_x \approx \sqrt{N}\hat{p}$ ,  $\hat{J}_y \approx J - \hat{c}^\dagger \hat{c}$  and  $\hat{J}_z \approx \sqrt{N}\hat{x}$ . Here,  $\hat{c}^\dagger$  denotes a bosonic mode creation operator, and  $\hat{x}$  and  $\hat{p}$  the corresponding position and momentum quadratures, respectively. Consequently, the TACT Hamiltonian can be approximated by  $\hat{H} = \chi(\hat{J}_x^2 - \hat{J}_z^2) \approx -\chi N[(\hat{c}^\dagger)^2 + \hat{c}^2]$ . Similarly, for the LMG model (at  $\delta/\chi N = 1/2$ ) near the saddle point,  $H = \chi \hat{J}_z^2 + \frac{\chi N}{2} \hat{J}_y \approx \chi N \hat{x}^2 - \frac{\chi N}{2} \hat{c}^\dagger \hat{c} \approx \chi N[(\hat{c}^\dagger)^2 + \hat{c}^2]$ , thereby locally resembling the TACT Hamiltonian.

#### Four-photon spectroscopy

Figure 1e shows the spectroscopic result for the four-photon resonance. For this experiment, we prepared two different initial Bloch vectors to be  $\pi/4$  above or below the equator with projections nominally along  $\hat{y}$ , as shown in Extended Data Fig. 1. When on resonance with  $\delta = 0$ , the ratio of the two dressing-laser amplitudes was balanced to achieve an effective Hamiltonian in the form  $\hat{H} = \chi \hat{J}_x^2$ , which preserves the azimuthal angle.

The four-photon detuning  $\delta$  can be intuitively understood as inducing a time-dependent OAT interaction  $\hat{H} = \chi \hat{J}_{\phi(t)}^2$  where the twisting axis rotates as  $\hat{J}_{\phi(t)} = \cos(\delta t/2)\hat{J}_x + \sin(\delta t/2)\hat{J}_y$ . With the four-photon detuning  $\delta \gg \chi N$ , the effective Hamiltonian recovered to the exchange interaction  $\hat{H} = \chi(\hat{\mathbf{J}} \cdot \hat{\mathbf{J}} - \hat{J}_z^2)$ , which induced finite changes in the azimuthal angle of the initial Bloch vectors with the signs depending on the initial projection along  $\hat{z}$ .

With a different set of initial states, the four-photon resonance can also be witnessed by the change in polar angle or equivalently spin projection  $J_z$ . In this experiment, we prepared initial Bloch vectors on the equator but with different azimuthal angles  $\phi = -\pi/4, 0$  and  $+\pi/4$ , as shown in Extended Data Fig. 2.

When on resonance with  $\delta = 0$ , the effective Hamiltonian  $\hat{H} = \chi \hat{J}_x^2$  caused a positive or negative change in  $J_z$  for initial states with  $\phi = \pm\pi/4$ . For  $\phi = 0$  the initial Bloch vector was along  $\hat{J}_x$ , which commutes with the Hamiltonian and, thus, experienced no change in  $J_z$ . When  $\delta \gg \chi N$ ,  $J_z$  was conserved under the effective exchange interaction  $\hat{H} = \chi(\hat{\mathbf{J}} \cdot \hat{\mathbf{J}} - \hat{J}_z^2)$  for all three initial states.

#### Sequences for measuring the flow vectors

The local flow vectors were measured by the changes in polar angles  $d\theta$  and azimuthal angles  $d\phi$ . Starting with all atoms in  $|\uparrow\rangle$ , the initial states were prepared by applying Bragg pulses with durations and phases determined by the initial state parameterized by  $\theta_i$  and  $\phi_i$ . For all the Bragg pulses applied, the Rabi frequency was 8.3 kHz, giving to a  $\pi$ -pulse duration of 60  $\mu$ s. Right after preparing the initial state, the interaction was applied before the wave packets separated. To measure the changes to the polar angles, we applied a  $\pi$ -pulse along  $\phi_i$ , adjusted the delay time to refocus the wave packets, applied a final  $(\pi/2 + \theta_i)$ -pulse along the axis  $\phi_i + 180^\circ$  to bring the Bloch vector nominally around to the equator and measured the projection of the Bloch vector  $J_{z|\Delta\theta}$  along  $\hat{z}$ . To measure the changes to the azimuthal angles, after the interaction, we applied a  $\pi$ -pulse around  $\phi_i$ , again adjusted the delay time to refocus the wave packets, applied a final  $\pi/2$ -pulse around  $\phi_i + 90^\circ$  and measured the projection of the Bloch vector  $J_{z|\Delta\phi}$  along  $\hat{z}$ . With the two sequences described above, the changes to the polar and azimuthal angles were mapped to the changes in the projection along  $\hat{z}$ , which were then estimated with  $d\theta = J_{z|\Delta\theta}/J$  and  $d\phi = J_{z|\Delta\phi}/J$ .

#### Dynamics around the unstable saddle point

Figure 3 shows the measured local flow vector as a function of the initial displacements from the unstable saddle point. For a more explicit comparison, the measurement data (left) and the corresponding numerical

simulation results (right) are shown in Extended Data Fig. 3. The original data and the corresponding simulation are presented in the top row, and the result after subtracting the superradiance is shown at the bottom. In both cases, we found clear agreement between theory and experiment.

For the measurement data, we estimated the effect of superradiance by averaging the displacement along  $\hat{z}$  for all data points. This common background displacement  $\delta J_z/N = 0.03$  was then subtracted from all points. For the numerical simulation, we considered the classical phase space structure for general XYZ models as discussed in ‘Mean-field equation of motion and stability analysis’ but with superradiance included. Now, the equations of motion become

$$\begin{aligned} \frac{dJ_x}{dt} &= 2\chi_y J_y J_z - \Gamma J_x J_z, \\ \frac{dJ_y}{dt} &= -2\chi_x J_x J_z - \Gamma J_y J_z, \\ \frac{dJ_z}{dt} &= 2(\chi_x - \chi_y) J_x J_y + \Gamma(J_x^2 + J_y^2). \end{aligned} \quad (14)$$

Here,

$$\Gamma = \kappa \left( \frac{g_0^2}{4\Delta_a} \right)^2 \left( \frac{|\alpha_1|^2}{\Delta_{c1}^2 + \kappa^2/4} - \frac{|\alpha_2|^2}{\Delta_{c2}^2 + \kappa^2/4} \right)$$

is the mean-field strength of the superradiance, which can be cancelled by balancing the intra-cavity powers of the two dressing-laser tones. The numerical simulation result based on equation (14) is presented in the top right of Extended Data Fig. 3. The simulation result with superradiance subtracted is shown in the bottom right. The subtraction was performed following the same procedure of subtracting the superradiance used in analysing the experimental data. The ratio  $\Gamma/\chi x = 0.2$  used in the simulation was determined by the detuning of the dressing-laser tone from the cavity resonance.

#### Initial state preparation

Starting with about  $10^8$  atoms in a magneto-optical trap near the cavity centre, we first applied polarization gradient cooling to load about  $2 \times 10^5$  atoms into the 813-nm red-detuned optical lattice. After ramping down the lattice depth,  $\Lambda$ -enhanced grey molasses cooling was applied to reduce the ensemble temperature down to 6  $\mu$ K. We then performed degenerate Raman sideband cooling to lower the radial temperature down to less than 1  $\mu$ K. Further optical pumping was applied to transfer the atom into the  $|F = 2, m_F = 0\rangle$  state, which resulted in a radial temperature of 1.4(5)  $\mu$ K (ref. 39).

About 1,000 atoms were selected with momentum spread  $\Delta p < 0.1\hbar k$  using velocity-selective two-photon Raman transitions. The remaining atoms were then removed with transverse radiation pressure<sup>39</sup>. To enhance the interaction with the more favourable Clebsch–Gordan coefficients, the atoms were transferred from  $|F = 2, m_F = 0\rangle$  to  $|F = 2, m_F = 2\rangle$  using a series of microwave pulses<sup>18</sup>, leading to a single-particle cooperativity  $C = 1.37$ .

#### Generating frequency tones for rotations and interactions

Quantum non-demolition measurements and Bragg rotations of momentum states were realized by a single laser coupled into the cavity<sup>18</sup>. We refer to this laser as the atomic probe. It was stabilized to the blue of the atomic transition  $\omega_a$  with a detuning of about 500 MHz.

Driving Bragg rotations between  $|p_0 - \hbar k\rangle$  and  $|p_0 + \hbar k\rangle$  required two different laser tones separated by  $\omega_z$ . These two tones were generated by first redshifting the atomic probe frequency by 75 MHz with an acousto-optic modulator (AOM) and then blueshifting it back with another AOM driven with two radio-frequency (RF) tones

at  $\omega_{\text{RF1}} = 2\pi \times 75$  MHz and  $\omega_{\text{RF2}} = (2\pi \times 75 - \omega_z)$  MHz. The phase of the Bragg rotation  $\phi_B = \phi_{\text{RF2}} - \phi_{\text{RF1}}$  was defined by the relative RF phases of  $\omega_{\text{RF2}}$  and  $\omega_{\text{RF1}}$ . To compensate for the changing Doppler shift due to the free-falling, the frequency separation between the two tones was chirped by  $25.11 \text{ kHz ms}^{-1}$ .

To drive the interactions, we needed two tones offset by  $2\omega_z$  with the separation chirped by  $50.22 \text{ kHz ms}^{-1}$ . This was again realized by first redshifting the atomic probe by 75 MHz with one AOM and then blueshifting it back with another AOM. In this case, the second AOM was driven by two RF tones at  $\omega_{\text{RF1}}$  and  $\omega_{\text{RF3}} = (2\pi \times 75 - 2\omega_z)$  MHz. Here,  $\omega_{\text{RF3}} = 2\omega_{\text{RF2}} - \omega_{\text{RF1}}$  was generated by first frequency-doubling  $\omega_{\text{RF2}}$  then mixing with  $\omega_{\text{RF1}}$  to shift the frequency back down after proper frequency filtering. By doing so, we maintained the differential phase  $\phi_{\text{int}} = (\phi_{\text{RF3}} - \phi_{\text{RF1}})/2 - \phi_B$  between the Bragg rotations and the interactions were stabilized. This differential phase could be rapidly controlled by the RF phase of  $\omega_{\text{RF2}}$ .

### Data availability

The datasets generated during and analysed during the current study are available in the CU Scholar repository, with the identifier <https://doi.org/10.25810/kkbc-wm40>.

### Acknowledgements

This material is based upon work supported by the US Department of Energy, Office of Science, National Quantum Information Science Research Centers, Quantum Systems Accelerator. We also acknowledge funding support from the Vannevar Bush Faculty Fellowship, the National Science Foundation (Grant Nos. 2317149 (Physics Frontier Center), PHY-2309135 to the Kavli Institute

for Theoretical Physics (KITP) and OMA-2016244 (QLCI)), the Heising-Simons Foundation and NIST. We acknowledge helpful discussions with K. Mølmer and V. Vuletić and useful feedback from M. Marinelli and C. Miller.

### Author contributions

C.L. and C.M. contributed to the building of the experiment and capturing and analysing the data. J.K.T. conceived and supervised the experiments. H.Z. and A.C. contributed to the theoretical derivation and numerical simulations and were supervised by A.M.R. C.L., H.Z., A.M.R. and J.K.T. wrote the manuscript. All authors discussed the experiment implementation and results and contributed to the manuscript.

### Competing interests

The authors declare no competing interests.

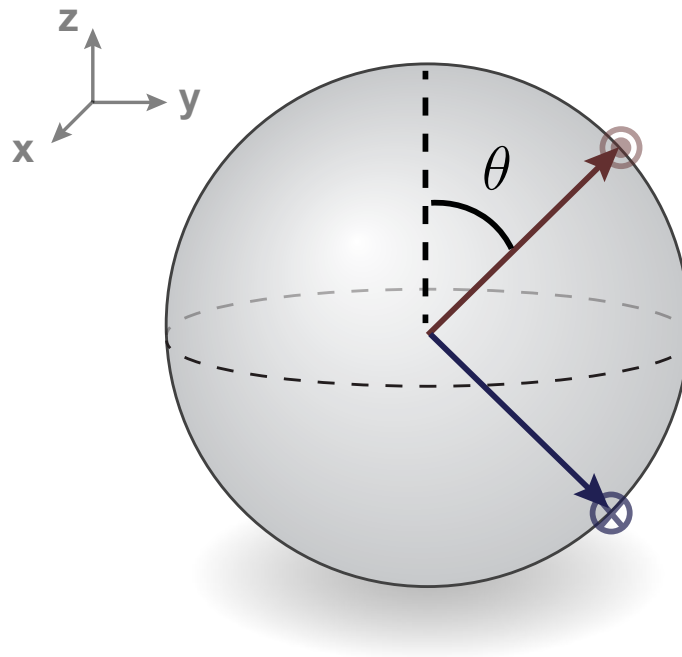
### Additional information

**Extended data** is available for this paper at <https://doi.org/10.1038/s41567-025-02866-0>.

**Correspondence and requests for materials** should be addressed to James K. Thompson.

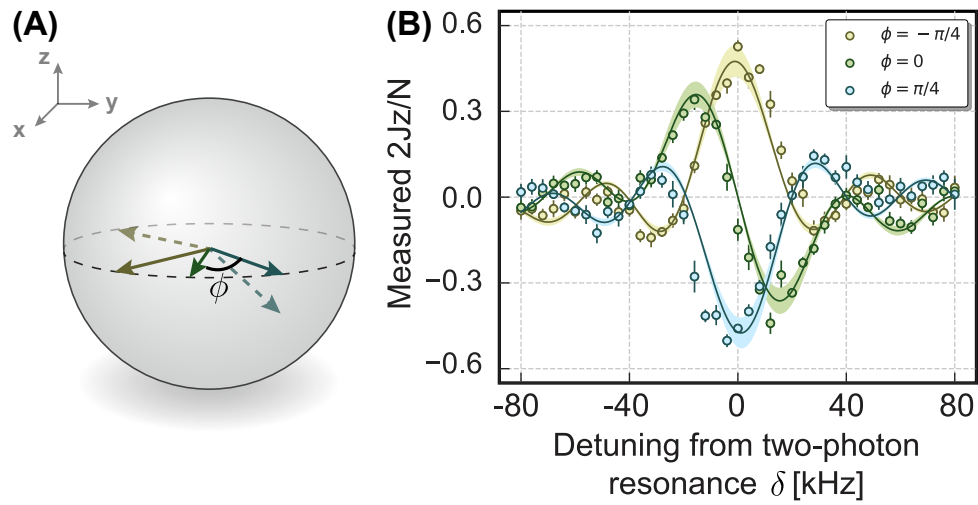
**Peer review information** *Nature Physics* thanks the anonymous reviewers for their contribution to the peer review of this work.

**Reprints and permissions information** is available at [www.nature.com/reprints](http://www.nature.com/reprints).



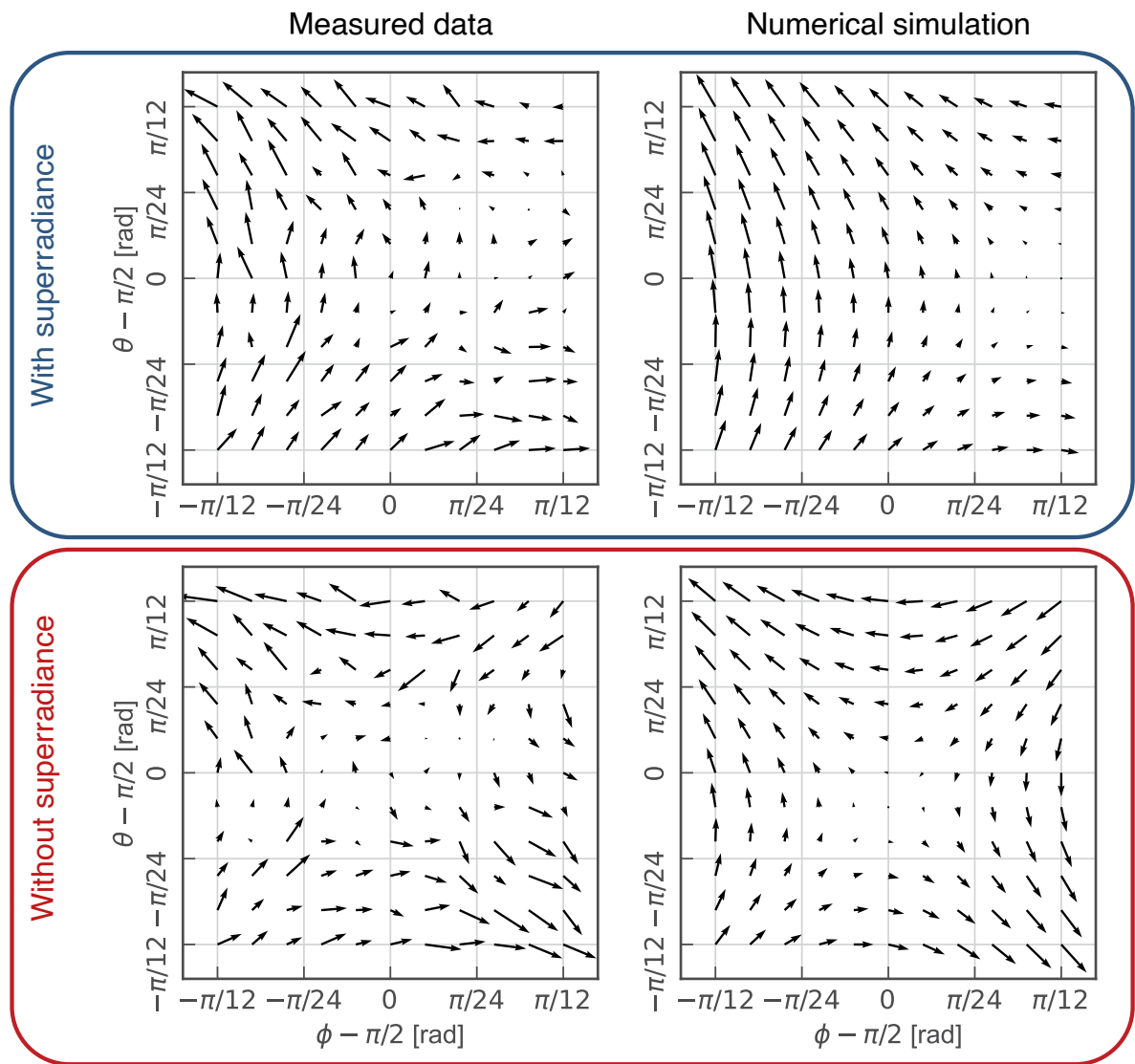
**Extended Data Fig. 1 | Initial states for four-photon spectroscopy.** Bloch sphere representation of the initial states used in the four-photon spectroscopy experiment. The initial Bloch vectors are prepared with polar angles  $\theta = \pi/4$  (red) and  $\theta = 3\pi/4$  (blue) in the  $y-z$  plane. At the mean-field level, the exchange

interaction induces an azimuthal phase shift that rotates the initial Bloch vectors into (blue cross) or out of (red dot) the page. The coordinate axes are labeled as  $\hat{x}$ ,  $\hat{y}$ , and  $\hat{z}$ .



**Extended Data Fig. 2 | Four-photon spectroscopy with initial states on the equator.** (A) The initial Bloch vectors. (B) Interaction induced change in  $Jz$  as a function of the four-photon detuning for initial Bloch vectors with different

azimuthal angles  $\phi = -\pi/4$ ,  $0$  and  $+\pi/4$  (yellow, green and blue circles). Data is fit with 68% confidence band and all error bars presented are  $1\sigma$  uncertainties derived from 40 experimental trials.



**Extended Data Fig. 3 | Experimentally measured local flow (upper) and numerical simulation result (lower).** We present the data before (right) and after (left) subtracting the superradiance, which both match with the theory. Here,  $\theta$  and  $\phi$  are the polar and azimuthal angle of the initial Bloch vector.